

# RANS-BASED SUB-SCALE MODELLING IN EDDY-RESOLVING SIMULATION METHODS

S. Jakirlić, M. Bopp, C-Y. Chang, F. Köhler, B. Krumbein, L. Kutej, D. Kütemeier, I. Maden, R. Maduta, M. Ullrich, S. Wegt and C. Tropea

*Institute of Fluid Mechanics and Aerodynamics, Technical University of Darmstadt  
Alarich-Weiss-Straße 10, D-64287 Darmstadt, Germany*

`jakirlic@sla.tu-darmstadt.de`

## Abstract

The activities of the group for 'Modelling and Simulation of Turbulent Flows' at the Institute of Fluid Mechanics and Aerodynamics (Technical University of Darmstadt, Germany) in hybridizing the RANS (Reynolds-Averaged Navier-Stokes) and LES (Large-Eddy Simulation) computational methods for simulating complex turbulent flows are reviewed.

## 1 Introduction

All turbulent flows are inherently unsteady. Even if the mean flow can be regarded as steady (and e.g. two-dimensional) the turbulence is always unsteady (and three-dimensional). In some simple attached flows, the mean flow and corresponding turbulence structure can be correctly captured by using conventional models employed in (steady/unsteady) RANS (Reynolds-Averaged Navier Stokes) framework. However, in configurations featured e.g. by flow separated from curved continuous walls (characterized by intermittent separation region) the fluctuating turbulence associated with a highly unsteady separated shear layer has to be adequately (to an appropriate extent) resolved in order to capture even the mean flow properties correctly. Accordingly, the application of a suitable scale-resolving turbulence model is required. The flow complexity is especially enhanced when dealing with high Reynolds number flows. Extremely high demands on spatial and temporal resolutions prevent the application of highly feasible computational methods, such as Direct Numerical Simulation (DNS) and Large-Eddy Simulation (LES). Furthermore, a highly irregular anisotropic grid cells' arrangement, not only in the immediate wall vicinity, invalidates the Smagorinsky-related subgrid-scale models, keeping in mind an explicit dependence of the stresses residing in subgrid scales ( $\tau_{ij} \propto \nu_{sgs} S_{ij}$ ) on the grid spacing, corresponding directly to the filter width. Especially suitable for handling such complex flows, also at higher Reynolds numbers, are the hybrid RANS/LES (Large-Eddy Simulation) methods. Their aim is to combine the advantages of both RANS and LES methods in order to provide a computational procedure that is capable to affordably capture the unsteadiness of the flow. Unlike in the LES framework utilizing mostly the SGS (SubGrid-Scale) models of the Smagorinsky type (0-equation models), where the grid spacing  $\Delta$  represents the characteristic size of the largest unresolved scales (subgrid-scales),

the representative length (and time) scales of the residual turbulence entering the relevant equations of motion in the hybrid LES/RANS methodologies are determined by solving respective equations describing the dynamics of corresponding turbulence quantities. Accordingly, the basic of any Hybrid RANS/LES method is a RANS-based model formulation describing the unresolved sub-scale fraction of turbulence. The RANS-based sub-scale models of different complexity are appropriately 'sensitized' to account for turbulence unsteadiness (fluctuating turbulence) by introducing either:

- a grid-spacing-dependent filter parameter: mostly in the length-scale determining equation - PANS (Partially-Averaged Navier-Stokes, proposed principally by Girimaji, 2006 and further developed by Basara et al., 2011, 2018) / PITM (Partially-Integrated Transport Model, developed principally by Chaouat and Schiestel, 2005), equation/expression - DES-related schemes (DES - Detached-Eddy Simulation, developed principally by Spalart et al., 1997; see also Spalart, 2009 for further upgrades) / VLES (Very LES; proposed principally by Speziale, 1998;)  
or
- the von Karman length scale  $L_{vK} = \kappa S / |\nabla^2 U|$  - nominally a grid-spacing-free model formulation; SAS - related models (Scale-Adaptive Simulation model developed principally by Menter and Egorov, 2010)

Accordingly, the model equations (formulated and validated within the Steady RANS framework, describing the fully-modeled turbulence) adapt automatically (by interplaying with the grid resolution) to the highly-unsteady (unresolved, residual) sub-scale turbulence. The grid spacing incorporated in the hybrid LES/RANS models, represents just one of several model parameters serving for the determination of the unresolved turbulent scales. The relevant model formulations point to complex relationships involving different turbulent quantities exhibiting high level of coherence. Consequently, unlike in the LES method, where the grid size  $\Delta$  influences very directly the final outcome, the grid spacing  $\Delta$  is obviously a less influential factor in Hybrid LES/RANS models - such a model rationale has inherently much more physics, allowing the use of coarser spatial and temporal resolutions.

## 2 Presently used eddy-resolving models

Following eddy-resolving computational models are presently in focus<sup>1</sup>:

- **VLES** (Very Large-Eddy Simulation) and **PANS** (Partially-Averaged Navier Stokes) - seamless, variable resolution hybrid LES/RANS models (Chang et al., 2014; Chang et al., 2015b; Jakirlic et al., 2014, 2016a, 2016b, 2017, 2018, Krumbein et al., 2017a, 2017b, 2018). In both methods a four-equation ERM-based model formulation (Elliptic-Relaxation Method), solving the equation describing the dynamics of the normal-to-wall turbulence intensity component in addition to equations governing the sub-scale kinetic energy of turbulence and its dissipation rate (Hanjalic et al., 2004), was employed to mimic the sub-scale model seamlessly in the entire flow domain. Whereas the destruction term in the equation governing the scale-supplying variable is appropriately modelled in the PANS framework, the VLES method is concerned with appropriate suppression of the turbulent viscosity in the equation of motion directly. Such actions cause turbulence level to be suppressed towards the 'subscale' ('sub-filter') level. Herewith, the development of the structural characteristics of the flow and associated turbulence is enabled.
- An **eddy-resolving Reynolds-stress model** (RSM) for unsteady flow computations: denoted as Instability-sensitive RSM - IS-RSM (Jakirlic and Maduta, 2015a, 2015b; Maden et al., 2015; Maduta et al., 2017; Kütemeier et al., 2019; Köhler et al., 2020; Bauer et al., 2020). The model scheme adopted, functioning as a 'sub-scale' model in the Unsteady RANS framework, represents a differential near-wall Reynolds stress model formulated in conjunction with the scale-supplying equation governing the homogeneous part of the inverse turbulent time scale. The model capability to account for the vortex length and time scales variability was enabled through a selective enhancement of the production of the dissipation rate in line with the SAS proposal (Menter and Egorov, 2010) pertinent particularly to the highly unsteady separated shear layer regions. Recently, the SAS-relevant methodological sensitivity towards adequate capturing of the turbulence instabilities is extended to an eddy-viscosity model. Similar as in both PANS and VLES methods the Hanjalic et al. (2004) model formulation has been appropriately modified, Krum-

<sup>1</sup>A **zonal two-layer hybrid LES/RANS methodology** (it could also be considered as a **RANS-based wall-modelled LES**), with a differential near-wall eddy-viscosity model covering the wall layer and the conventional LES resolving the core flow, represents also a relevant research activity (Jakirlic et al., 2009, 2010 and 2011). Special attention was devoted to the coupling of both methods, the issue being closely connected to the treatment at the interface separating RANS and LES sub-regions. Hereby, great importance is attached to simplicity, efficiency and applicability to complex geometries. The exchange of the variables across the LES/RANS interface was adjusted by implicit imposition of the condition of equality of the modelled turbulent viscosities (by assuming the continuity of their resolved contributions across the interface), enabling a smooth transition from RANS layer to the LES sub-region. Next important issue is the utilization of a self-adjusting interface position in the course of the simulation. A control parameter representing the ratio of the modelled (SGS) to the total turbulent kinetic energy in the LES region, averaged over all grid cells at the interface on the LES side, is adopted in the present zonal modelling strategy.

bein et al. (2020). The model proposed is denoted as the **eddy-resolving ERM-based eddy-viscosity model** (denoted by  $ER-\zeta-f$ ). The initially proposed SAS-formulation involving the von Karman length scale ( $L_{vK} = (\kappa S/|\nabla^2 U|)$ ), was reformulated here by expressing it as a function of the second derivative of the velocity field directly, as proposed originally by Rotta (1972). The latter modification, making the model even more sensitive against turbulence unsteadiness (a resolving mode can be enabled at even coarser grid resolutions), has been consequently used also in conjunction with the previously mentioned Reynolds-stress model, Kütemeier et al., 2019; Köhler et al., 2020; Bauer et al., 2020. Both URANS-based sub-scale model formulations are grid-spacing free unlike the majority of relevant hybrid RANS/LES models, representing certainly an advantage, especially if unstructured grids with arbitrary grid-cell topology are to be employed.

The predictive performances of the proposed models are intensively validated in numerous aerodynamic-type flows of different complexity featured by boundary layer separation, swirl and impinging, including also convective heat transfer cases. A selection of relevant results as well as the results obtained by the consequent models application to some configurations relevant to car aerodynamics and IC engines is illustrated in Section 3. All VLES and IS-RSM model equations are implemented into the OpenFOAM Code with which all respective computations have been performed, whereas the AVL-FIRE [1] code was applied for all PANS computations. In all cases second-order accurate spatial and temporal discretization schemes have been applied.

## 3 Computational illustrations

Selected results illustrating the predictive capabilities of the afore-introduced RANS-based eddy-resolving models are displayed in the following figures without going into specific details with respect to the flow configurations description, spatial (grid size and arrangement) and temporal resolutions, discretization methods, inflow and boundary conditions; for all these details interested readers are referred to respective publications.

### 3.1 PANS-related results

The predictive performance of the PANS methodology is preliminary investigated by computing a series of canonical, geometrically simpler configurations, but featured by complex flow straining and associated turbulent interactions including separation, swirling effects and mean compression in a square piston-duct assembly, Chang et al. (2015a, 2015b). The results shown presently are exclusively related to the external car aerodynamics (Jakirlic et al., 2016b, 2018). Figures 1-6 illustrate the feasibility of the PANS method in computing the flow past three 'DrivAer' car models (Heft et al., 2012; Heft 2014) characterized by differently designed rear end shapes: estate-back, fastback and notchback configurations. Fig. 1 depicts the vortex structure past the estate-back model visualized by using the Q-criterion.

The vortex structure refinement associated with an intensive unsteadiness in the wake behind the car can be observed. The near-wake region is populated with smaller vortices whereas the ligament-like vortices shedding from the car surface experience a certain disruption caused by a complex flow straining in the far wake region.

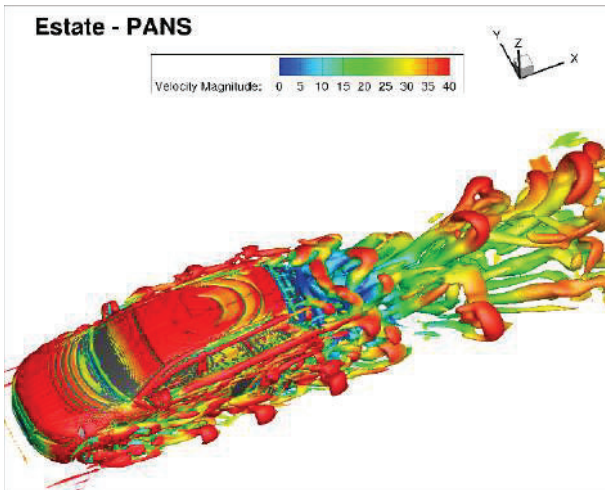


Figure 1: Q-criterion visualization of the vortex structure past the estate-back configuration predicted by PANS method ( $Q = 6500s^{-2}$ )

The appropriately high resolution of the structural characteristics of the wake region led to its intensive spreading pointing to an enhanced turbulence activity, complying with the PANS method's capability to capture fluctuating turbulence to a corresponding extent. Figures 2 show the PANS-related mean velocity field and associated streamlines illustrating the separation region behind the estate-back and fast back 'DrivAer' car models.

Whereas the fastback and notchback (not shown here) models are characterized by a very similar wake topology, the estate back configuration points to a much more complex vortex system. The correspondingly large flow reversal region occupying the entire box-type rear-end originates from the boundary layer separating in parallel (in the spatial sense) from the roof edge over its entire spanwise extent, sides and underbody. Accordingly, a complex vortical pattern is formed consisting of two pairs of counter-rotating vortices: the base vortices interacting with the ground (encountered also in both the notchback and fast-back configurations) and the so-called tip vortices. The surface pressure distribution (Fig. 3) at the car body is completely in accordance with the computed velocity field exhibiting total deceleration within the stagnation region occupying the front part (characterized by  $C_p = 1$ ) followed by high acceleration at the strongly curved front car surface associated with a steep  $C_p$  decrease. After the pressure alternation from a characteristic rise at the engine cover surface and a further pressure drop reflecting the effects of the favourable pressure gradient due to a flow acceleration over the front window a certain plateau characterized by negative values pertinent to the roof surface is reached. Apart of the roof locality accommodating the wall-mounted sting (not accounted for in the computational study), the agreement with the experimental results is very good. The  $C_p$ -developments related to three investigated rear end designs start to differ from each other approximately at the middle of the roof. Whereas a negative pressure plateau characterizes the estate-back configuration preceding a sudden jump to an almost zero  $C_p$ -value related to a relatively steep transition from the roof to the rear-window, the pressure development at the notchback and fastback car models exhibits a much more complex trend. The relevant pressure progressions are qualitatively similar, but the distinct positive peak values are spatially

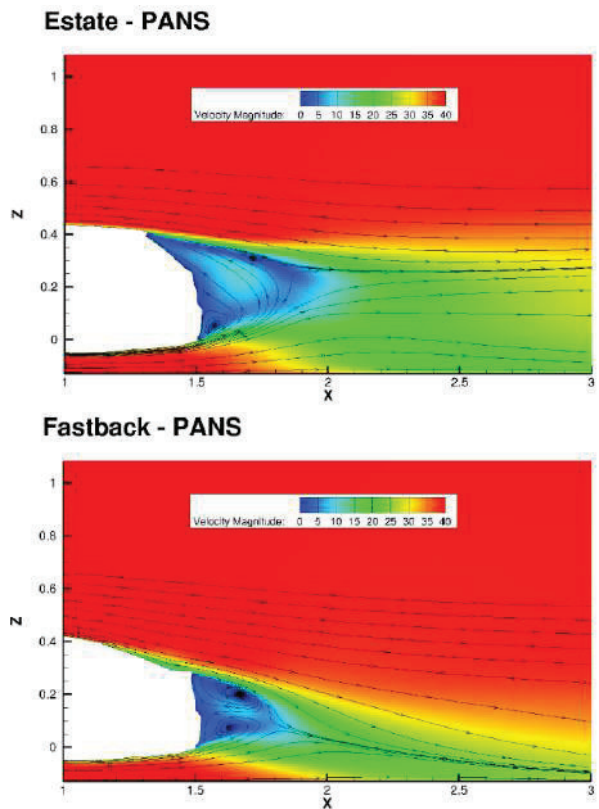


Figure 2: Estate-back and fastback 'DrivAer' car models: mean streamlines and iso-contours of the velocity field colored by its magnitude obtained by the PANS method

shifted, with that related to the fastback model occurring more downstream, following the turnover of the velocity field from accelerating to decelerating mode.

A qualitative impression about the flow past a BMW car model taking over a truck model is illustrated in Fig. 4. Both vehicles represent down-scaled (1:2.5), geometrically-similar models of realistic vehicle configurations for which on-road measurements have been performed by Schrefl (2008). Figures 5 display the Q-criterion visualization of the vortical flow structure corresponding to two car-truck relative positions  $x/L = -0.80$  and  $x/L = 0.39$ , with the latter relating to the most critical car-truck constellation characterized by the largest drag coefficient. Between these positions a characteristic change of the drag coefficient from reduced to enlarged

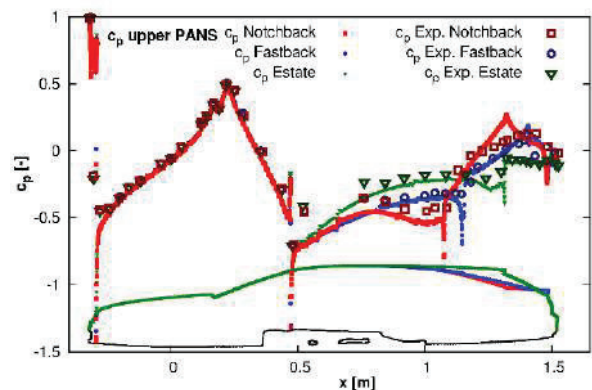


Figure 3: Development of the mean surface pressure coefficient over the upper surface of all three investigated configurations - notchback, fastback and estate-back

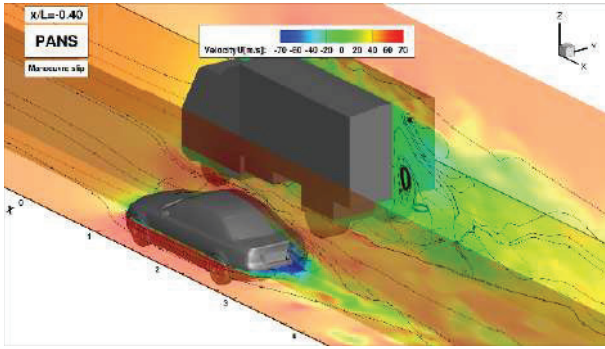


Figure 4: Computationally obtained instantaneous velocity field and corresponding streamlines related to the car-truck relative position  $x/L = -0.40$

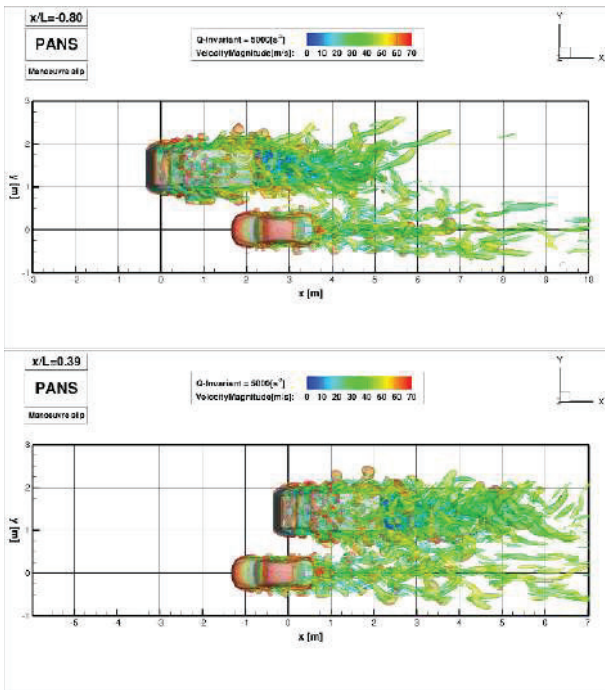


Figure 5: Computationally obtained vortex structures related to the car-truck relative positions  $x/L = -0.80$  (upper) and  $0.39$  (lower) visualized by the Q-criterion

value relative to the isolated single car occurs (investigated by Jakirlic et al., 2014). The inherent flow unsteadiness originating from the multiple stagnation regions at the front end of both vehicles, front side of the wheels and mirrors remained preserved down to the far wake region. These pictures indicate also the spatial extent of the vortical structures in terms of their size and shape diversity, similar to those displayed in Fig. 1. The complex flow straining expressed through an intensified interaction between wall-bounded and subsequent multiple separated shear layers influences strongly the formation of the wake region. Similar as in the case of the 'DrivAer' model (Fig. 1) the adequate capturing of the intensified turbulence activity within the wake requires an appropriately high resolution of the related structural properties, representing the inherent feature of the PANS methodology. Figures 6 show the development of the aerodynamic coefficients associated with the side force ( $F_s$ ), representing the spanwise ( $y$ ) component of the force comprising contributions originating from both the pressure and friction forces, and the yawing moment ( $C_{Mz}$ ). The PANS results are obtained

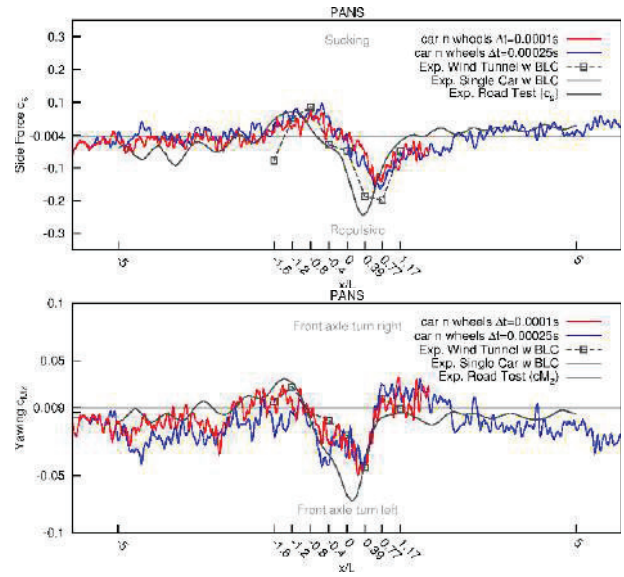


Figure 6: Variation of the car-related aerodynamic coefficients associated with the side force ( $C_s$ ) and yawing moment ( $C_{Mz}$ ) during the overtaking manoeuvre

by applying two temporal resolutions corresponding to time steps  $\Delta t = 0.0001\text{sec}$  and  $\Delta t = 0.00025\text{sec}$ . The solid black lines displaying the development of both coefficients represent the experimental results determined during the 'on-road' overtaking process involving realistic vehicles. The prime focus of the experimental campaign was the investigation of the car stability during the 'on-road' overtaking manoeuvre, characterized by strong unsteadiness of the oncoming flow. Accordingly, only these two mostly relevant quantities have been measured. In addition, the quasi-steady wind-tunnel measurements, represented by the square symbols, are used here as a reference. Both coefficients follow closely the experimental reference. Outside of the 'overtaking region' (taking place between  $x/L = -1.60$  and  $x/L = 1.17$ ) both coefficients oscillate weakly about the value corresponding closely to that related to the isolated single car (marked by the horizontal line). The flow acceleration, and consequently the pressure reduction, within the gap between two vehicles is especially pronounced at the relative position  $x/L = -0.80$  corresponding to the highest positive value of the side force directed towards the truck (Fig. 6-upper). This effect, representing an expected outcome complying with the car situated in the truck wake characterized by lower flow velocities, implies the truck exerting a suction effect on the car. Analysis of the yawing moment development (Fig. 6-lower), the maximum value of which is reached somewhat earlier compared to the side force, reveals a complementary reaction: the car's front axle is turned into right direction towards the truck. In the further course of the overtaking process a dramatic change of both coefficients, from positive to negative values, takes place. The side force coefficient experiences its lowest (negative) value at the relative position  $x/L = 0.39$ ; the minimum negative value of the yawing moment is recorded earlier, at the position  $x/L \approx 0.0$ . The flow within the narrow gap is still accelerated, but there is a bow-wave effect originating from the truck acting repulsively on the car. This process is complemented by the front axle turning into left direction away from the truck, being in relation with the negative yawing moment.

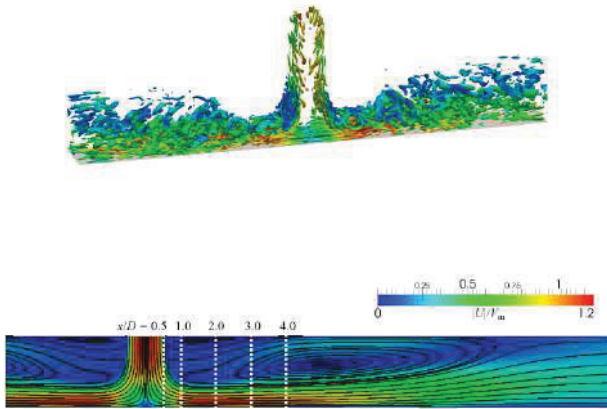


Figure 7: Q-criterion-visualization of the vortical structure in the impinging jet flow coloured by velocity magnitude (upper), mean velocity field and corresponding streamlines (lower)

### 3.2 VLES-related results

In the course of the VLES model development different canonical flows have been computed: natural decay of the homogenous isotropic turbulence, channel flow in a Reynolds number range (also over a rough surface, Krumbein et al., 2017a) and separated flow over a curved continuous surface, Chang et al. (2014). The method is consequently applied to a swirling flow in cooling hole of a turbine blade as well as to different vehicle aerodynamics cases, Jakirlic et al. (2016a, 2017). Here, some selected results related to a slot-jet impinging perpendicularly onto a heated wall and thermal mixing in a cross-stream type T-junction (Krumbein et al., 2017b, 2018) will be presented.

Fig. 7 shows the vortex structure of the plane jet at  $Re_m = 9120$  impinging onto a heated wall visualized by Q-criterion and the resulting mean velocity field with corresponding streamlines. The strong deceleration of the jet by approaching the bottom plate related to the stagnation region and subsequent acceleration and wall-jet formation are clearly visible. A large recirculation zone with a very low back-flow intensity is created at the upper wall.

Figures 8 show the semi-log plots of the mean velocity and temperature profiles obtained by the VLES and RANS (employing the  $\zeta - f$  model representing the RANS constituents of the VLES) methods along with the DNS results (Hattori and Nagano, 2004) at selected streamwise  $x/D$ -locations (marked by dashed lines in Fig. 7). Fig. 8-upper shows the velocity in the near-wall region normalized by the local wall friction velocity  $U_\tau$  varying in streamwise direction. The displayed mean velocity profile development reveals very strong departure from the equilibrium conditions, underlying the logarithmic law. The high positive pressure gradient typical of the impingement region (streamwise position  $X/D = 0.5$ ) causes large departure from the log-law in line with the strong jet deceleration when perpendicularly impinging the wall. The consequent flow relaxation in terms of the mean velocity intensification (flow acceleration) pertinent to the wall jet region is documented at the positions  $x/D = 1 - 4$  in very good

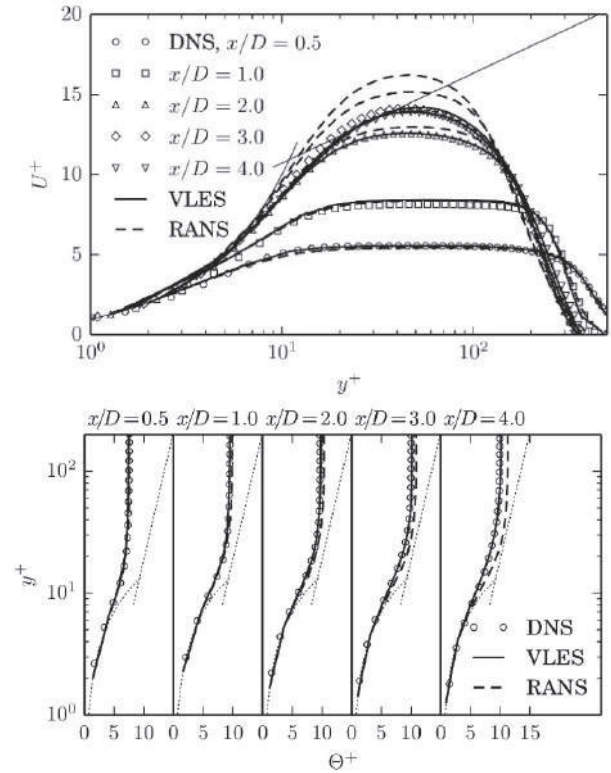


Figure 8: Velocity and temperature profiles in wall units at different locations  $x/D$ . For better visibility, only every third data point of the DNS data set is shown

agreement with the DNS database. With the RANS model a slight overprediction of the velocity at the more upstream positions is obtained. Regarding the thermal fields, mean temperature field is analysed. Fig. 8-lower shows temperature profiles in wall units at different positions along the impingement plate. The temperature is non-dimensionalized by normalizing the difference of the temperature and the local wall temperature ( $T - T_w$ ) with the friction temperature  $\theta_\tau = q_w / (\rho C_p U_\tau)$ . Again a highly non-equilibrium nature of the thermal field considered is clearly illustrated by a corresponding departure from the conditions associated with the logarithmic law. Very good agreement is obtained with the VLES model, while the RANS model overpredicts slightly the temperature away from the wall at further downstream positions.

Thermal mixing in two cross-stream T-junction configurations occurring under constant (DNS reference by Hattori et al., 2014) and variable (experimental reference by Hirota et al., 2010) fluid properties is presently considered. Here, as an illustration, only the results related to the former configuration will be shown, Figure 9-11 (for more details Krumbein et al. 2018 should be consulted). The flow field arising from the impingement of the two crossing streams is displayed in Fig. 9. The flow issuing from the vertical branch-channel detaches at its right upper edge denoted by position  $x/H = 0.0$ ; subsequently, a flow reversal zone is developed at the lower main-channel-wall with associated flow acceleration in the upper part of the channel complying with the continuity condition. The separated shear layer aligned with the mean dividing streamline is primarily responsible for a strong turbulence production - the most intensive turbulence activity originates from the separation process (see Fig. 10). Further downstream at  $x/H = 2$ , the flow reattaches. The Q-criterion image ( $Q = 10s^{-2}$ ) enables

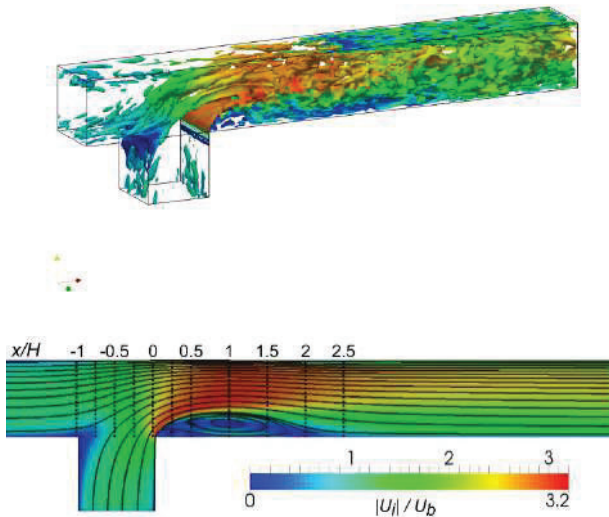


Figure 9: Q-criterion-visualization of the vortical structure in the T-junction configuration coloured by velocity magnitude (upper), mean velocity field and corresponding streamlines (lower)

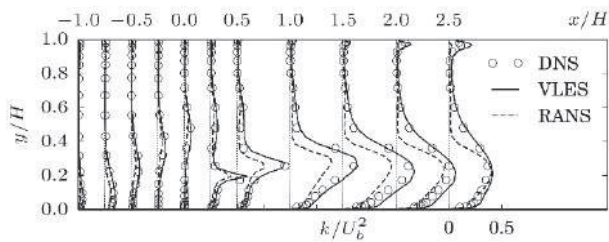


Figure 10: Turbulence kinetic energy profiles normalized by the bulk velocity at different streamwise positions

visualization of the mechanisms of the separated shear layer generation at the right edge of the vertical branch channel dominated by the spanwise vorticity, its rolling up and finally its shedding and disruption by a correspondingly complex straining within the main horizontal channel. The profiles of the kinetic energy of turbulence (Fig. 10) and appropriately normalized mean temperatures (Fig. 11) are evaluated at different streamwise positions  $x/H$  marked by the dotted lines in Fig. 9. The results interpretation covers all characteristic flow localities: crossing/merging zone of main and branch streams, recirculation zone including separation and reattachment points, as well as the post-reattachment region. Typical turbulent intensity field is obtained revealing the strong profiles' asymmetry with characteristic near-wall

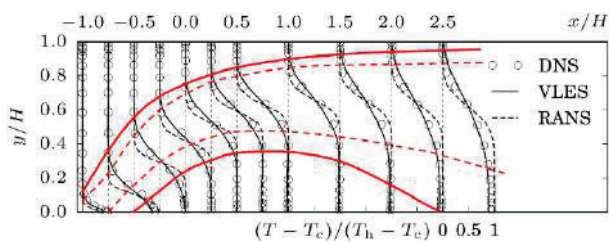


Figure 11: Temperature profiles normalized with hot and cold stream temperatures at different streamwise positions (red lines denote the thermal layer spreading)

peaks representing the consequence of enhanced turbulence production due to the strong velocity gradients at both bottom and upper walls, and the intensified turbulence activity at the wall distances coinciding with the separated shear layer region. Overall good agreement between the VLES and DNS data can be observed. The  $\zeta - f$ -RANS model underpredicts the turbulence level, especially in the separated shear layer region and the recirculation bubble. The underestimation of the turbulence kinetic energy in the separated shear layer is, as it is well-known, associated with a weaker momentum transfer into the recirculation zone representing the prime reason for the overestimation of the length of the recirculation bubble. The thermal layer area characterized by large temperature gradients (Fig. 11) progresses above the separated shear layer representing the region where the thermal streams originating from both inflow channels merge. Thermal mixing is captured accurately within the VLES framework. In the RANS simulation however, thermal mixing intensity is severely underpredicted resulting in a too narrow thermal mixing layer, characterized by a too steep temperature gradient with corresponding underestimation of temperature level in the upper and overestimation in the lower part of the main channel. This points to a weaker momentum exchange and consequently a lower spreading rate of the separated shear layer; the latter outcome is, as discussed earlier, directly correlated with the lower turbulence activity in this region.

### 3.3 IS-RSM-related results

Numerous canonical attached flows and flows separated from sharp-edged and curved walls have been computed in the course of interactive model development and validation, Jakirlic and Maduta (2015a, 2015b). Figures 12-23 offer a relevant overview illustrating the feasibility of the model in simulating flows of enhanced complexity subjected to different extra strain rates relevant e.g. to plasma-actuated flow control towards the pressure recovery enhancement in a 3D diffuser (Maden et al., 2015), flow and aeroacoustics past a tandem cylinder (Maduta et al., 2017; Köhler et al., 2020), dynamic stall effects at a plunging airfoil (Kütermeier et al., 2019) and pulsating flow in an aortic aneurysm (Bauer et al., 2020).

Flow in the 3D diffuser is extremely complex, Fig. 12. It is characterized by a 3D separation bubble starting in the corner built by two expanding walls (blue area). Initial growth of this corner bubble reveals its spreading rate along two sloped walls being approximately of the same intensity. As the adverse pressure gradient along the upper wall significantly outweighs the one along the side wall due to a substantially higher angle of expansion,  $11.3^\circ$  vs  $2.56^\circ$ , the separation zone spreads gradually over the entire top wall surface. The strong three-dimensional nature of the separation pattern is obvious.

The pulsed forcing imparted by the plasma actuator (PA; mounted on the upper wall of the inflow duct) to the fluid flow in the spanwise direction, generating a pair of the streamwise vortices, changes completely the natural sense of the rotational pattern of the secondary motion in inflow duct as well as its intensity, Fig. 13. The orientation of the PA-generated vortex in the upper duct corner opposes a fairly weak vortex in the lower duct corner, with the latter still resembling the orientation of the baseline secondary motion. The relevant peak transverse velocity magnitude is about ten times higher compared to the baseline configuration and about twenty times higher in the case of continuous ac-

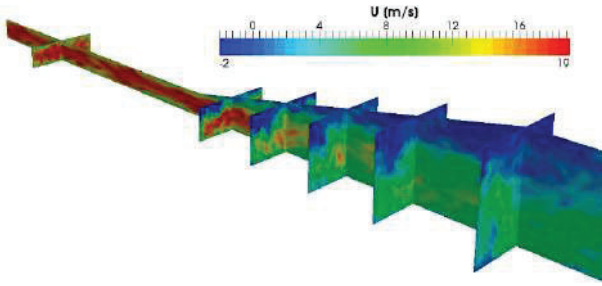


Figure 12: Flow in a 3D diffuser, baseline configuration - instantaneous velocity field

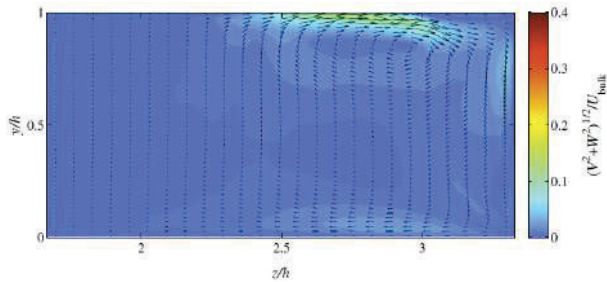


Figure 13: Flow in a 3D diffuser, plasma-actuated configuration (pulsed mode with 40% duty cycle) - time-averaged velocity field coloured by velocity magnitude and corresponding velocity vectors in the cross-section of the inflow duct (only one half is shown)

tuation (not shown here). Depending on the operating mode, the plasma-actuated manipulation of the inflow conditions modifies secondary flow structure selectively, either towards an increase of the turbulence intensity, as in the case of pulsed actuation, or towards its suppression, as it is characteristic for the continuous operation. The modification of the secondary motion through the plasma actuator reflects restructuring of the separated flow within the diffuser, see Fig. 14. The turbulence intensity in the duct wall boundary layer transforming into a separated shear layer is closely correlated with the size of the flow reversal zone: higher turbulence level implies a higher momentum transport across the separated shear layer and a consequent depletion of the recirculation bubble. Accordingly, whereas the recirculation zone occupies the entire upper wall in the diffuser section and consequently a part of the straight duct (Fig. 12) in the baseline flow, the flow reversal vanishes almost completely in the case of the actuator pulsed with 40% duty cycle, Fig. 14-left. In the continuous actuation case, the lower turbulence intensity influenced by significant secondary flow acceleration in the region corresponding to the actuator location causes the flow to separate at the side diffuser wall (Fig. 14-right), unlike in the baseline case.

Fig. 15 illustrates the development of the pressure coefficient on the bottom wall of the 3D diffuser configuration representing the practically most important outcome of the actuation. In all three diffuser configurations the continuous pressure decrease in the inflow duct is followed by a steep increase after entering the diffuser section. The different pressure recovery levels depend strongly on the mode of the plasma-based actuation of the secondary vortices in the inflow duct. The pressure recovery enhancement for the pulsed configuration is obvious compared to the baseline case without flow control. Accordingly, it represents the most efficient actuation, contributing to a strong turbulence activity

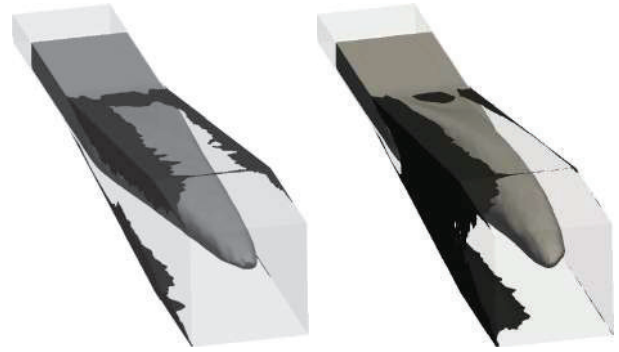


Figure 14: Iso-surfaces of axial velocity component  $U/U_{bulk} = -0.01$  (black iso-surface) and  $0.4$  (gray iso-surface) for two plasma-actuated diffuser cases with pulsed mode (left; 40% duty cycle) and continuous mode (right; 100% duty cycle)

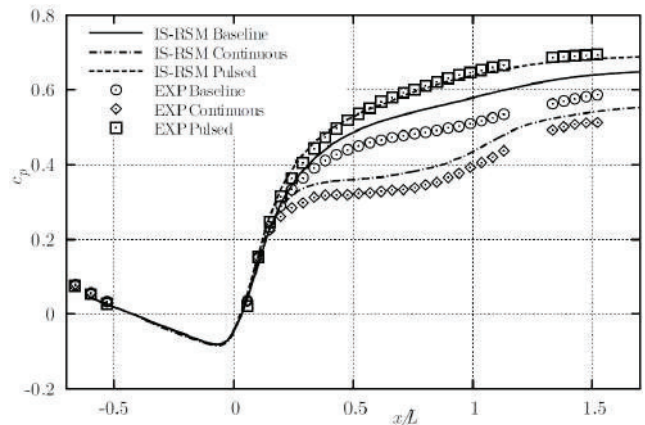


Figure 15: Flow in a 3D diffuser - Pressure coefficient distribution at the bottom diffuser wall for baseline and actuated cases (experiment by Grundmann et al., 2011)

intensification and causing significant reduction of the cross-sectional area occupied by the flow reversal.

Fig. 16 illustrates the instantaneous flow field past an in-line arrangement of a tandem cylinder visualized by the Q-criterion. The IS-RSM model's capability of resolving the turbulence unsteadiness enables development of turbulent structures in the gap and wake regions; the complex vortex shedding process and associated flow features are returned quantitatively accurate. The quantitative evidence of the results obtained by both conventional RSM and IS-RSM models is verified by contrasting their outcome along with the experimentally obtained results (Lockard et al., 2007; Neuhart et al., 2009), Figures 17-18. The tandem cylinder configuration can be regarded as a simplified version of a landing gear and can therefore serve as the first step in testing turbulence models for predicting the airframe noise. The unsteady pressure field is the most important flow variable acting as the noise-source representative. Conventional RANS models fail traditionally in predicting it because of their time-averaging rationale. Only unsteady interactions involving large scales can be reasonably captured. The unsteady feature of the pressure field is represented through the root-mean-square of the fluctuating pressure on downstream cylinder, Fig. 17. The model results are compared to those of the tripped experiments. It was experimentally found that the second cylinder is the main source of noise as the relevant  $C'_{P'_{rsm}}$  values are four to five times higher than those measured on the upstream

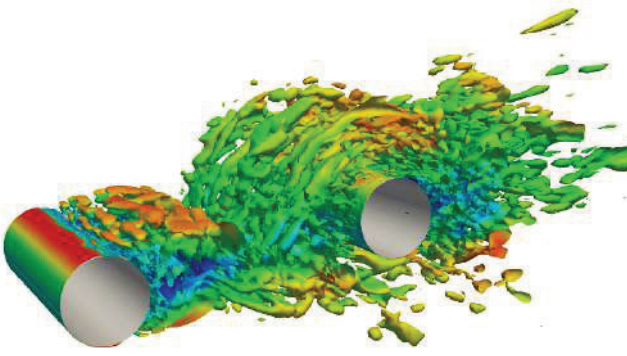


Figure 16: Instantaneous flow structure visualized by the Q-criterion (Q - iso-surfaces are coloured by the streamwise velocity magnitude) computed by the IS-RSM

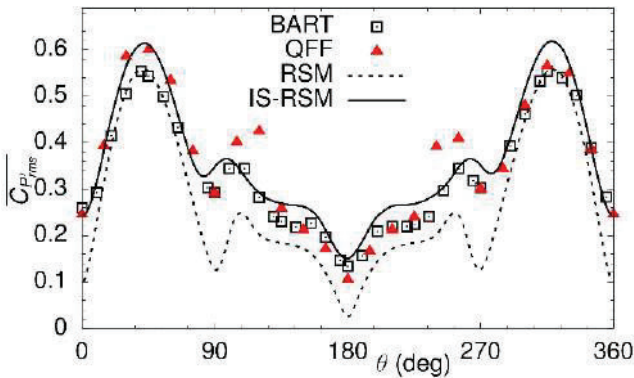


Figure 17: Root-mean-square (rms) of the fluctuating pressure at the downstream cylinder obtained by both conventional RSM and its instability-sensitive variant

cylinder. The IS-RSM model results exhibit reasonable agreement in regard to both peak values and  $\overline{C_p'_{rms}}$  distribution over the most of the cylinder surface, indicating the model's high potential for being used as a tool for the noise prediction. The RSM model results in a qualitatively correct shape of the  $\overline{C_p'_{rms}}$  distribution but underestimates significantly its values at the entire cylinder surface. Obviously that incapability of capturing the small-scale unsteadiness and their interaction with the large scales caused such a non-satisfactory outcome.

The time-dependent flow features are illustrated further in relation to the frequency spectrum of the surface pressure at  $\theta = 45^\circ$  at the downstream cylinder in Fig. 18-upper by the power spectral density (PSD). The IS-RSM results exhibit very good agreement with the QFF data while the RSM computations, due to the time-averaged rationale of the URANS approach, reproduce substantially lower PSD level with distinct discrete peaks, because only a weak unsteadiness of the large-scale motion could be resolved. Furthermore, the primary vortex shedding frequency corresponds to 190.3 Hz in relation to the RSM-related computation and 172.5 Hz to the IS-RSM-related one, with the latter comparing very well with the frequency of 178 Hz evaluated experimentally.

The power spectral density of the acoustic pressure following from the aeroacoustic computations based on the unsteady flow fields is presented for the far-field microphone position B in Fig. 18-lower (the results for microphones A and C are similar, but are not shown here for the sake of brevity). The PSD resulting from the IS-RSM computation is in very good agreement with

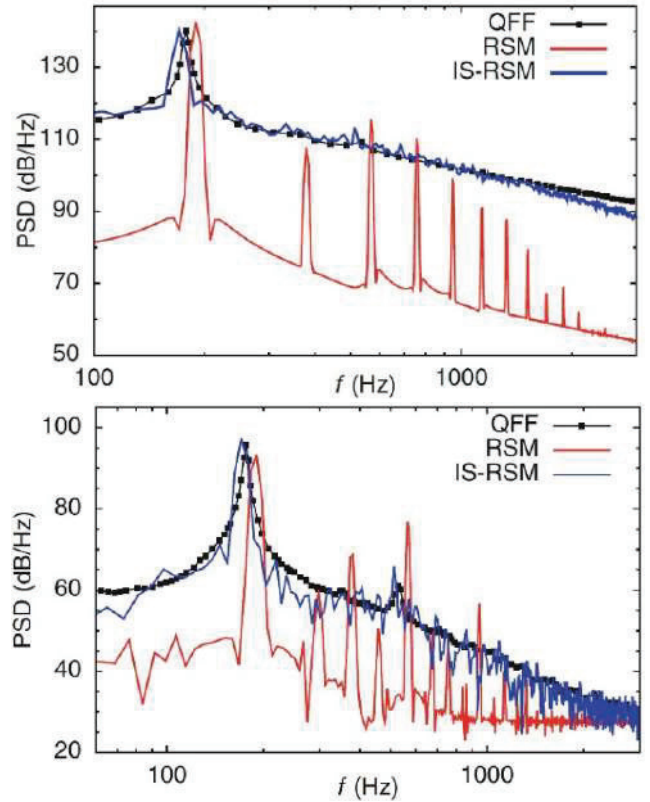


Figure 18: PSD of the surface pressure at  $\theta = 45^\circ$  on the downstream cylinder (upper) and far-field noise illustrated by the PSD of acoustic pressure at microphone position B (lower)

the experimental data over the entire frequency range matching both the PSD peak value and the corresponding frequency quite well, unlike the RSM-related PSD result. The acoustic results, corresponding closely to the previously displayed PSD of the surface pressure, support the conclusion that the IS-RSM computations can generate appropriate acoustic sources in the flow field representing highly suitable background for reasonable determination and analysis of the far-field noise.

The next computational example deals with a plunging airfoil down-stroke-motion causing a vertical velocity component being imposed to the free stream velocity in an airfoil-fixed frame of reference, which implies a change of the effective angle of attack  $\alpha_{eff}$ . When  $\alpha_{eff}$  reaches a specific threshold, determined by the airfoil's leading edge curvature, the boundary layer rolls up and forms a leading-edge vortex (LEV) that accumulates negative vorticity ( $\omega^-$ ). The topology of the vortex growth and detachment phase can be described by a combination of half saddles, full saddles and nodes as identifiers as outlined by Rival et al. (2014), Fig. 19. Topologically, the LEV is bounded by two half saddles, one at the leading edge where the LEV is fed by the separated shear layer, and one at the rear reattachment point. While the LEV grows by accumulating mass, its reattachment point travels downstream until it reaches the trailing edge, Fig. 19a. In case of the presently considered boundary-layer eruption mechanism the LEV induces an adverse pressure gradient on the boundary layer that forms on the airfoil's surface below the vortex towards the leading edge. When the velocity induced by the rotating LEV increases, the adverse pressure gradient reaches a critical value. Consequently, the boundary-layer beneath the vortex will separate and eject fluid of

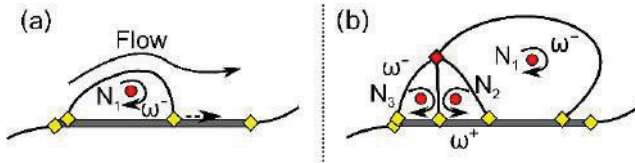


Figure 19: Boundary layer eruption mechanism: half saddle (yellow-coloured diamond), full saddle (red-coloured diamond) and node (N; red-coloured circle) - (a) growing LEV and (b) separation into primary (N1), secondary (N2) and tertiary (N3) vortex

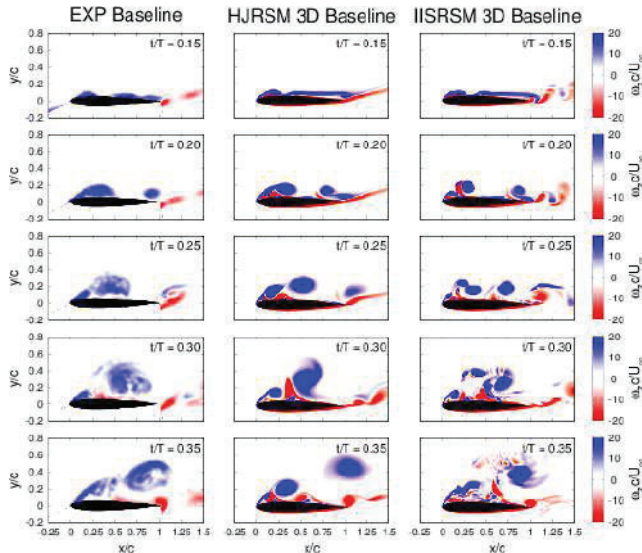


Figure 20: Temporal variation of the normalized spanwise vorticity of the LEV generated at a plunging airfoil

positive signed vorticity ( $\omega^+$ ) between vortex and leading edge. This upward ejection forms a secondary vortex termed N2 rotating opposite ( $\omega^+$ ) of the LEV ( $\omega^-$ ), Fig. 19b. To satisfy topological consistency, a tertiary vortex N3 ( $\omega^-$ ) arises ahead of the secondary vortex.

Figures 20 and 21, illustrating the temporal evolution of the spanwise vorticities and corresponding lift coefficient, compare directly the results obtained by three-dimensional computations employing both the baseline (HJ)RSM model and its eddy-resolving IIS-RSM counterpart with the experimental reference (Rival et al., 2014). The vorticity measurements represent the results of a 'single-shot' experiment (the computations are performed in the same way); the experimentally obtained  $C_L$ -coefficient represents an average over ten realisations.

The flow field obtained by the instability-sensitive IIS-RSM model has, unlike the flow field related to the HJ-RSM model employed within the conventional URANS procedure (featured by a very weak bulk flow unsteadiness in the spanwise direction), a true three-dimensional character, representing the outcome complying with the capability of the IISRSM model of capturing the turbulence fluctuations, also in the spanwise direction. The vorticity field (averaged over the spanwise direction; Fig. 20), depicted at the same time sequences as those obtained by the HJ-RSM model, show much finer structure. It is characterized by a somewhat longer sustainment of the shear layer feeding the Leading-Edge-Vortex, reflected also in a closer agreement of the lift coefficient with the experimental reference; this relates mostly to the decreasing part of the lift coefficient development, Fig. 21.

The final presently considered configuration focuses on

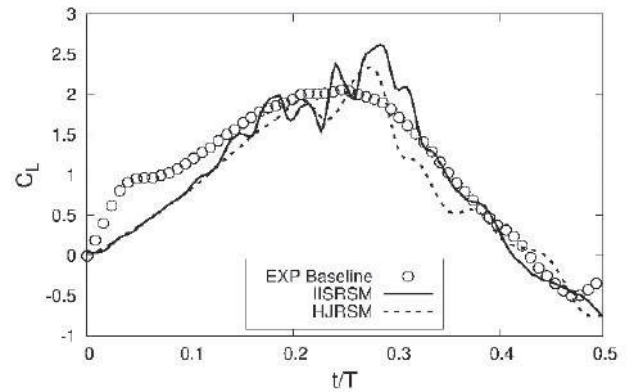


Figure 21: Temporal development of the lift coefficient

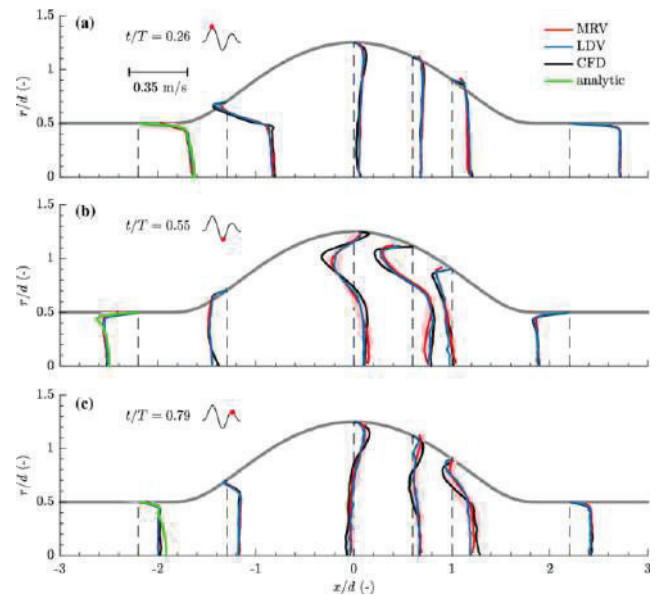


Figure 22: Spatial development of the mean axial velocity profile at the three time steps of peak volume flow rate

the physiologically pulsating flow in an aortic aneurysm for which the experimental reference has been provided (by employing the MRV and LDV measurement techniques) by Bauer et al. (2020), Figures 22-23.

Fig. 22 displays the mean axial velocity profile development within the aneurysm configuration at the three time steps corresponding to peak volume flow rates, acquired with MRV and LDV, compared to the CFD-IISRSM result and an analytic (laminar flow) solution. The temporal evolution of the flow resembling a physiological variation of the volume flow rate in the aorta, shown in small diagram in the upper left corner, relates to the so-called exercise conditions. The 'positive' peak flow Reynolds number (measured at the time instant  $t/T = 0.26$ ) is 7649, whereas the one related to the 'negative' peak (at  $t/T = 0.55$ ) corresponds approximately to 5550. The shaded red area indicates the variation of the MRV velocity profiles over the circumferential direction. The velocity field is typical of a pulsating flow with alternating reversal flow regions. Overall agreement between experimental and computational results is on a very high level. At the time instant  $t/T = 0.26$  the flow detaches at the proximal neck due to the increasing flow rate forming a vortex ring which subsequently induces negative velocities at the wall, expands over the entire aneurysm cross-sectional area, travels downstream, weakens and finally

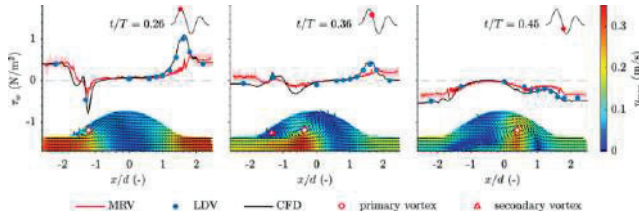


Figure 23: Spatial distribution of the WSS for different time steps during the cycle (with the corresponding values depicted on the left axis). The respective flow rate at each time step is denoted by red point in the upper right corners. The MRV-related circumferentially-averaged velocity field is given on the bottom (using the right colourbar and the lower axis)

dissipates. This vortex ring growth can be adequately followed in Fig. 23, highlighting also the generation and movement of both primary and secondary vortex cores in the flow field. In addition, the spatial distribution of the wall shear stress (WSS) at different time sequences within one physiological cycle is shown. Its alternating behaviour is closely correlated with the previously illustrated velocity field. The simulation results exhibit very good agreement with the LDV measurement, while the MRV results show some underestimations, especially in the regions and at the time steps where high WSS peaks are present.

## 4 Summary

An overview of the activities is presented related to development and application of differently-designed RANS-based eddy-resolving strategies for turbulent flow simulations, relying on both eddy-viscosity and Reynolds-stress modelling concepts. Numerous highly non-equilibrium flow configurations exhibiting different features is computationally studied and discussed along with reference experiments and other (LES/DNS) computational studies demonstrating the model feasibility and applicability in a broad range of complex, wall-bounded turbulent flows.

## Acknowledgements

We acknowledge the financial support of the German Scientific Foundation (DFG-TRR150-B03; TR 194/56-1 and HE 1875/30-1), Federal Ministry for Economic Affairs and Energy (BMW, GRS Project No. 1501417 and AiF-FVV IGF-Project No. 20224 N/2), EU Project ATAAC (with the grant number ACP8-GA-2009-233710) and the AVL List GmbH (Graz, Austria). Our special thanks go to Dr. Branislav Basara for an intensive cooperation in relation to the AVL-FIRE Code application and the PANS modelling strategy.

## References

[1] AVL-FIRE Programme Manual, AVL List GmbH, Graz, Austria. CFD Solver Version 2017.1

[2] Basara, B., Krajnovic, S., Girimaji, S. and Pavlovic, Z. (2011): Near-Wall Formulation of the Partially Averaged Navier-Stokes Turbulence Model. *AIAA Journal* 49(12): 2627-2636

[3] Basara, B., Pavlovic, Z. and Girimaji, S. (2018): A new approach for the calculation of the cut-off resolution parameter in bridging methods for turbulent flow simulation. *Int. J. Heat Fluid Flow* 74: 76-88

[4] Bauer, A., Bopp, M., Jakirlić, S., Tropea, C., Shokina, N., Krafft, A. and Hennig, J. (2020): Analysis of the wall shear stress in a generic aneurysm under pulsating and transitional flow conditions. *Experiments in Fluids* 61(2):59, doi: 10.1007/s00348-020-2901-4

[5] Chang, C.-Y., Jakirlic, S., Dietrich, K., Basara, B. and Tropea, C. (2014): Swirling flow in a tube with variably-shaped outlet orifices: an LES and VLES study. *Int. J. Heat and Fluid Flow* 49:28-42, doi: 10.1016/j.ijheatfluidflow.2014.05.008

[6] Chang, C.-Y., Jakirlić, S., Basara, B. and Tropea, C. (2015a): Predictive capability assessment of the PANS- model of turbulence. Part I: physical rationale by reference to wall-bounded flows including separation. In "Advances in Hybrid RANS-LES Modelling 5". Notes on Numerical Fluid Mechanics and Multidisciplinary Design, Vol. 130, S. Girimaji et al. (Eds.), pp. 371-383, doi: 10.1007/978-3-319-15141-030

[7] Chang, C.-Y., Jakirlić, S., Basara, B. and Tropea, C. (2015b): Predictive capability assessment of the PANS- model of turbulence. Part II: application to swirling and tumble/mean-compression flows. In "Advances in Hybrid RANS-LES Modelling 5". Notes on Numerical Fluid Mechanics and Multidisciplinary Design, Vol. 130, S. Girimaji et al. (Eds.), pp. 385-398, doi: 10.1007/978-3-319-15141-031

[8] Chaouat, B. and Schiestel, R. (2005): A new partially integrated transport model for subgrid-scale stresses and dissipation rate for turbulent developing flows. *Phys. Fluids* 17 (065106): 1-19

[9] Girimaji, S.S. (2006): Partially-Averaged Navier-Stokes Model for Turbulence: A Reynolds-Averaged Navier-Stokes to Direct Numerical Simulation Bridging Method. *J. Appl. Mech.* 73: 413-421

[10] Grundmann, S., Sayles, E. Eaton, J.K. (2011): Sensitivity of an asymmetric 3D diffuser to plasma-actuator induced inlet condition perturbations. *Experiments in Fluids* 50(1): 217-231

[11] Hanjalić, K., Popovac, M. and Hadziabdić, M. (2004): A robust near-wall elliptic-relaxation eddy-viscosity turbulence model for CFD, *Int. J. Heat and Fluid Flow* 25: 1047-1051

[12] Hattori, H. and Nagano, Y. (2004): Direct numerical simulation of turbulent heat transfer in plane impinging jet. *Int. J. Heat and Fluid Flow* 25: 749-758

[13] Hattori, H., Iwase, M., Houra, T. and Tagawa, M. (2014): DNS and LES for turbulent heat transfer and mixing in T-junction channel flow. 10th Int. ERCOFTAC Symp. on Eng. Turbulence Modelling and Meas., Marbella, Spain.

[14] Heft, A., Indinger, T. and Adams, N. (2012): Introduction of a New Realistic Generic Car Model for Aerodynamic Investigations. *SAE Technical Paper* 2012-01-0168

- [15] Heft, A. (2014): Aerodynamic Investigation of the Cooling Requirements of Electric Vehicles, PhD Thesis, Technical University Munich, Verlag Dr. Hut, ISBN 978-3-8439-1765-0
- [16] Hirota, M., Mohri, E., Asano, H. and Goto, H. (2010): Experimental study on turbulent mixing process in cross-flow type T-junction. *Int. J. Heat and Fluid Flow* 31: 776-784
- [17] Jakirlić, S., Kniesner, B., Kadavelil, G., Gnirß, M. and Tropea, C. (2009): Experimental and computational investigations of flow and mixing in a single-annular combustor configuration. *Flow, Turbulence and Combustion* 83(3):425-448, doi: 10.1007/s10494-009-9229-8
- [18] Jakirlić, S., Kadavelil, G., Kornhaas, M., Schäfer, M., Sternel, D.C. and Tropea, C. (2010): Numerical and Physical Aspects in LES and Hybrid LES/RANS of Turbulent Flow Separation in a 3-D Diffuser. *Int. J. Heat and Fluid Flow* 31(5):820-832, doi: 10.1016/j.ijheatfluidflow.2010.05.004
- [19] Jakirlić, S., Kniesner, B. and Kadavelil, G. (2011): On interface issues in LES/RANS coupling strategies: a method for turbulence forcing. *JSME Journal of Fluid Science and Technology* 6(1):56-72, doi: 10.1299/jfst.6.56
- [20] Jakirlić, S., Kutej, L., Basara, B. and Tropea, C. (2014): Computational study of the aerodynamics of a realistic car model by means of RANS and hybrid RANS/LES approaches. *SAE International Journal of Passenger Cars - Mechanical Systems* 7(2):559-574, doi: 10.4271/2014-01-0594
- [21] Jakirlić, S. and Maduta, R. (2015a): Extending the bounds of "steady" RANS closures: towards an instability-sensitive Reynolds stress model. *Int. J. Heat and Fluid Flow* 51:175-194, doi: 10.1016/j.ijheatfluidflow.2014.09.003
- [22] Jakirlić, S. and Maduta, R. (2015b): Sensitized RANS modelling of turbulence: resolving turbulence unsteadiness by a (near-wall) Reynolds stress model. *Progress in Wall Turbulence 2: Understanding and Modeling*. M. Stanislas, J. Jimenez and I. Marusic (Eds.), pp. 17-35, Springer Verlag, ERCOFTAC Series Vol. 23, doi: 10.1007/978-3-319-20388-1\_2
- [23] Jakirlić, S., Kutej, L., Hanssmann, D., Basara, B. and Tropea, C. (2016a): Eddy-resolving Simulations of the Notchback DrivAer Model: Influence of Underbody Geometry and Wheels Rotation on Aerodynamic Behaviour; *SAE Technical Paper Series*, Paper No. 2016-01-1062, doi: 10.4271/2016-01-1602
- [24] Jakirlić, S., Kutej, L., Basara, B. and Tropea, C. (2016b): Numerische Fahrzeugaerodynamik am Beispiel von 'DrivAer' Modellkonfigurationen. *Automobiltechnische Zeitschrift - ATZ*, Band 118 (5/2016): 78-85, doi: 10.1007/s35148-016-0012-6 (also as Computational vehicle aerodynamics by reference to 'DrivAer' model configurations. *ATZ Worldwide*, Vol. 118 (5/2016): 76-83; doi: 10.1007/s38311-016-0008-6)
- [25] Jakirlić, S., Kutej, L., Unterlechner, P. and Tropea, C. (2017): Critical assessment of some popular scale-resolving turbulence models for vehicle aerodynamics. *SAE International Journal of Passenger Cars - Mechanical Systems* V126-6EJ 10(1):235-250, doi: 10.4271/2017-01-1532
- [26] Jakirlić, S., Kutej, L., Basara, B. and Tropea, C. (2018): Scale-resolving simulation of an 'on-road' overtaking maneuver involving model vehicles. *SAE Technical Paper Series*, Paper No. 2018-01-0706, doi: 10.4271/2018-01-0706
- [27] Köhler, F., Maduta, R., Krumbein, B. and Jakirlić, S. (2020): Scrutinizing Conventional and Eddy-resolving Unsteady RANS Approaches in Computing the Flow and Aeroacoustics past a Tandem Cylinder. "New Results in Numerical and Experimental Fluid Mechanics XII", Notes on Numerical Fluid Mechanics and Multidisciplinary Design (NNFM), Vol. 142, Dillmann, A. et al. (Eds.), pp. 586-596, doi: 10.1007/978-3-030-25253-3\_56
- [28] Krumbein, B., Fooroghi, P., Jakirlić, S., Magagnato, F. and Frohnäpfel, B. (2017a): VLES modeling of flow over walls with variably-shaped roughness by reference to complementary DNS. *Flow, Turbulence and Combustion* 99(3-4):685-703, doi: 10.1007/s10494-017-9867-1
- [29] Krumbein, B., Jakirlić, S. and Tropea, C. (2017b): VLES study of a jet impinging onto a heated wall. *Int. J. Heat and Fluid Flow* 68:290-297, doi: 10.1016/j.ijheatfluidflow.2017.09.020
- [30] Krumbein, B., Termini, V., Jakirlić, S. and Tropea, C. (2018): Flow and heat transfer in cross-stream type T-junctions: A computational study. *Int. J. Heat and Fluid Flow* 71:179-188, doi: 10.1016/j.ijheatfluidflow.2018.03.013
- [31] Krumbein, B., Maduta, R., Jakirlić, S. and Tropea, C. (2020): A scale-resolving elliptic-relaxation-based eddy-viscosity model: development and validation. "New Results in Numerical and Experimental Fluid Mechanics XII", Notes on Numerical Fluid Mechanics and Multidisciplinary Design (NNFM), Vol. 142, Dillmann, A. et al. (Eds.), pp. 90-100, doi: 10.1007/978-3-030-25253-3\_9
- [32] Kütemeier, D., Wegt, S., Maden, I., Kissing, J., Maduta, R., Kriegseis, J., Jakirlić, S. and Tropea, C. (2019): Plasma-actuated Lift Enhancement of a Plunging Airfoil: A Computational Study. Paper No. AIAA-2019-0305, *SciTech 2019*, San Diego, CA, USA, January 7-11, doi: 10.2514/6.2019-0305
- [33] Lockard, D.P., Khorrami, M.R., Choudhari, M.M., Hutcheson, F.V. and Brooks, T.F. (2007): Tandem cylinder noise predictions. *AIAA Paper* 2007-3450
- [34] Maden, I., Maduta, R., Kriegseis, J., Jakirlić, S., Grundmann, S. and Tropea, C. (2015): Plasma-actuated manipulation of secondary flow towards pressure recovery enhancement in a 3D diffuser modelled by an eddy-resolving second-moment closure. *Flow, Turbulence and Combustion* 95(2-3):377-398 doi: 10.1007/s10494-015-9641-1
- [35] Maduta, R., Ullrich, M., Jakirlić, S. (2017): Reynolds stress modelling of wake interference of two cylinders in tandem: conventional vs. eddy-resolving closure. *Int. J. Heat and Fluid Flow* 67B:139-148, doi: 10.1016/j.ijheatfluidflow.2017.07.012

- [36] Menter, F. and Egorov, Y. (2010): The Scale-adaptive Simulation method for unsteady turbulent flow predictions. Part 1: theory and model description. *Flow, Turbulence and Combustion* 85: 113-138
- [37] Neuhart, D.H., Jenkins, L.N., Choudhari, M.M. and Khorrami, M.R. (2009): Measurements of the flow field interaction between tandem cylinders. *AIAA Paper* 2009-3275
- [38] Rival, D., Kriegseis, J., Schaub, P., Widmann, A., Tropea C. (2014): Characteristic length scales for vortex detachment on plunging profiles with varying leading-edge geometry. *Exp. in Fluids* 55:1-8
- [39] Rotta, J. C., 1972. *Turbulente Strömungen. Eine Einführung in die Theorie und ihre Anwendung.* Teubner Verlag Stuttgart (ISBN-10: 3519023164; ISBN-13: 978-3519023166)
- [40] Schreffl, N. (2008): *Instationäre Aerodynamik von Kraftfahrzeugen - Aerodynamik bei Ueberholvorgang und boeigem Seitenwind.* PhD Thesis, Technical University of Darmstadt, Germany, Shaker Verlag Aachen, ISBN 978-3-8322-7010-0
- [41] Spalart, P.R., Jou, W.-H., Strelets, M., Allmaras, S. (1997): Comments on the feasibility of LES for wings and on a hybrid RANS/LES approach, 1st AFOSR Int. Conf. on DNS and LES. In: Liu, C., Liu, Z. (Eds.), *Advances in DNS/LES.* Columbus, OH, Greyden Press, pp. 137-147
- [42] Spalart, P.R. (2009): Detached-Eddy Simulation. *Annu. Rev. Fluid Mech.* 41: 181-202
- [43] Speziale, C.G. (1998): Turbulence modeling for time-dependent RANS and VLES: A review. *AIAA Journal* 36(2):173-184